https://doi.org/10.1016/j.ijhydene.2019.02.244

Combined Methane Reforming by Carbon Dioxide and Steam in Proton Conducting Solid Oxide Fuel Cells for Syngas/Power Co-generation

Bin Chen[1,2], Haoran Xu[2], Yuan Zhang[2,3], Feifei Dong[4], Peng Tan[2], Tianshou Zhao[5,*], Meng Ni[2,*]

[1] Institute of Deep Earth Sciences and Green Energy, Shenzhen University, Shenzhen 518060, China
[2] Building Energy Research Group, Department of Building and Real Estate, The Hong Kong Polytechnic University, Hung Hom, Kowloon, Hong Kong, China
[3] State Key Laboratory of Materials-Oriented Chemical Engineering, College of Chemical Engineering, Nanjing Tech University, No. 5 Xin Mofan Road, Nanjing 210009, P. R. China
[4] College of Light Industry and Chemical Engineering, Guangdong University of Technology, Guangzhou 510006, China
[5] Department of Mechanical and Aerospace Engineering, The Hong Kong University of Science and Technology, Hong Kong, China

Email:
metzhao@ust.hk (Prof. Zhao)
bsmengni@polyu.edu.hk (Prof. Ni)
Tel: 852-27664152; Fax: 852-27645131

Abstract

Methane and carbon dioxide mixture can be used as the fuel in a proton conducting solid oxide fuel cell (SOFC) for power/syngas co-generation and greenhouse gas reduction. However, carbon deposition and low conversion ratio are potential problems for this technology. Apart from using functional catalytic layer in the SOFC to enhance CH_4 dry reforming, adding H_2O into the fuel stream could facilitate the CH_4 conversion and enhance the co-generation performance of the SOFC. In this work, the effects of adding H_2O to the CO_2-CH_4 fuel on the performance of a tubular proton conducting SOFC are studied numerically. Results show that the CH_4 conversion is improved from 0.830 to 0.898 after adding 20% H_2O to the anode. Meanwhile, the current density is increased from 2832 A m^{-2} to 3064 A m^{-2} at 0.7 V. Sensitivity studies indicate that the H_2:CO ratio can be effectively controlled by the amount of H_2O addition and the H_2 starvation can be alleviated, especially at high current density conditions.

Keywords:

Steam reforming; Dry methane reforming; Syngas; Modelling; Solid oxide fuel cells; Proton conducting.

1. Introduction

Syngas, a mixture of mainly CO and H_2, is a clean alternative to fossil fuels and a useful feedstock for producing other valuable chemical products, such as methanol and dimethyl ether. Traditionally, syngas is produced through the well-established pathways including gasification of various carbon sources (biomass, sludge, coal, etc.) [1–3] and steam reforming of methane/natural gas/biogas. Among those technologies, methane steam reforming (MSR) is well developed and commercialized. The H_2: CO ratio is 3:1 by the MSR process Eq. 1:

$$CH_4 + H_2O \leftrightarrow CO + 3H_2 \quad \Delta H^0_{298K} = 206.3 \text{ kJ mol}^{-1} \tag{1}$$

Notably, the reforming process is accompanied by the reversible water gas shift reaction (WGSR):

$$CO + H_2O \leftrightarrow CO_2 + H_2 \quad \Delta H^0_{298K} = 41 \text{ kJ mol}^{-1} \tag{2}$$

Besides the steam reforming, other methane-to-syngas processes (or the combination of them) are also available, such as dry methane reforming (DMR) [4], with a H_2:CO ratio of 1:1.

$$CH_4 + CO_2 \rightarrow 2CO + 2H_2 \quad \Delta H^0_{298K} = 247 \text{ kJ mol}^{-1} \tag{3}$$

The smaller H_2:CO ratio of DMR is beneficial to the post processing of syngas for the production of CH_3OH and CH_3COOH with high chemical values [5]. In addition to this, the dry reforming process is gaining renewed attention also because the CO_2 (a greenhouse gas) can be utilized [6]. In the context of energy sustainability, efficient fuel-to-power devices such as solid oxide fuel cells are being extensively studied recently, especially in the application of syngas utilization for power generation [7,8]. Due to the fuel flexibility of SOFC, dry reforming can be readily incorporated into the SOFC anode when running on natural gas or biogas, of which CH_4 and CO_2 are the main constitutions. The high operating temperature (600–800 °C) and Ni based anodic catalysts of SOFC enable the direct reforming of CH_4, which can be converted to syngas *in-situ* and further oxidized to H_2O and CO_2 in SOFC for electricity

generation. These two features enable SOFC to be a promising technology for power and syngas co-generation if the consumption of H_2 and CO by SOFC can be well controlled.

Recently, SOFCs fuelled by CH_4:CO_2 mixture with direct dry reforming of methane in the anode is widely examined [9–11]. Sameshima et al. developed a Ni and gadolinium doped ceria based anode for SOFC running on 30%-60% CH_4-CO_2 mixture with a maximum power density of 334 mW cm^{-2} and the increase of CO_2 fraction is found to be detrimental to the power density [10]. Mishina et al. used the CaO addition to effectively improve the anode carbon resistance and the cell durability for the direct dry methane reforming in the anode [11]. Proton conducting SOFC (H-SOFC) are also being actively studied since it has the advantages of 1) no steam dilution problem at the anode which occurs in the conventional oxygen ion conducting SOFC and 2) suitable for lower working temperature operation. Wan et al. developed a La_2NiO_4 perovskite layer onto the anode of an H-SOFC to boost the dry reforming of methane for syngas and electricity co-generation [12]. Hua et al. incorporated a $Ni_{0.8}Co_{0.2}$-$La_{0.2}Ce_{0.8}O_{1.9}$ functional layer in their H-SOFC, achieving a 91.5% CO_2 conversion at 700 °C [13]. We also conducted a thermal-electrochemical modelling study on the dry reforming process in a tubular H-SOFC with a NiCo-CeO_2/ZrO_2 dry reforming layer, in which effects of operating parameters on the co-generation performance are investigated, in terms of syngas composition, CH_2/CO_2 conversion rate and power density [14].

However, it is also viewed that the conversion of methane by dry reforming is usually lower than that of steam reforming due to the thermodynamics limitations and it is not yet well commercialized [15]. The carbon deposition is another issue in the dry reforming SOFCs, generally via the methane cracking reaction and CO disproportionation reaction in the operating temperature of SOFC (500ºC~800ºC) [16]. The steam reforming reaction over Ni is less vulnerable to the carbon deposition issue [17]. For H-SOFCs, the addition of H_2O is more important to prevent carbon deposition as steam is electrochemically produced in the cathode,

instead of in the anode. In view of this, the combination of steam reforming and dry reforming could be more feasible and attractive due to the alleviated carbon deposition and higher conversion ratios than single reforming mode [18]. There are also research works attempting to apply proton conducting cermet to the anode of SOFC, which can absorb water *in-situ* to facilitate internal reforming of CH_4 and reduce the carbon deposition [19,20]. Therefore, it is advisable to introducing steam to assist the dry methane reforming process to overcome those issues, thus necessary to investigate the effects of steam on both the reforming and the electrochemical performance of H-SOFC. Here we numerically studied the combined reforming process of methane by both CO_2 and H_2O in an H-SOFC that integrates a methane reforming catalyst layer, serving for the syngas production by internal reforming, and meanwhile for electrical power co-generation by utilizing part of the syngas. The results indicate that the introduction of H_2O can effectively improve the conversion of CH_4 and the yield of H_2, which further leads to the 8.4% current density improvement. Impacts of H_2O fraction, working voltage and the fuel flow rate on the co-generation performance are also investigated.

2. Reactor design and model development

The design and specifications of the tubular H-SOFC used in the previous work [14] are adopted here for consistency, as the focus of this work is on the effects of steam addition in the fuel gas. Fig. 1 sketches the geometry and layered structure of the tubular SOFC with the dry reforming layer (DMR) applied on top of the fuel electrode. Detailed geometry specifications and definition of nomenclatures can be found in [14]. The materials used for each layer are also shown in Fig. 1. The DMR layer consists of 6 wt % NiCo bimetallic catalyst supported on porous CeO_2/ZrO_2 (80:20 by weight), in which the DMR reaction (Eq. 3) takes place. The anode-supported SOFC uses the Ni/$BaCe_{0.5}Zr_{0.3}Y_{0.2}O_{3-\delta}$ (BCZY) composite anode as the support (namely the fuel electrode), with BCZY as the proton conducting electrolyte and

BCZY/$Sm_{0.5}Sr_{0.5}CoO_{3-\delta}$ (SSC) as the composite air electrode. The chemical reactions considered in the fuel electrode are represented by Eq. 1–3. The electrochemical reactions for the oxidation of hydrogen and reduction of oxygen occur at the porous anode and cathode sides of the SOFC, respectively:

$$H_2 \rightarrow 2H^+ + 2e^- \tag{4}$$

$$2H^+ + \frac{1}{2}O_2 + 2e^- \rightarrow H_2O \tag{5}$$

The multi-physical model is extended from our previously established model [14,21,22], which includes 4 sub-models briefed below.

2.1 Electrochemical model

The electrochemical model is used to compute various overpotentials associated with electrochemical reactions and the transport of charges (protons and electrons). The classic Nernst equation is employed to compute the equilibrium potential of the H_2 electrochemical oxidation at standard pressure (1 atm) as shown in Eq. 6. The fundamental Butler-Volmer equations as shown in Eq. 7–8 are used to correlate the activation loss $\eta_{act.a/c}$ with the current source $i_{source.a/c}$ produced by the anodic half-reaction (subscripted by "a") and cathodic half-reaction (subscripted by "c"), respectively:

$$E_{H_2} = 1.253 - 0.00024516T \tag{6}$$

$$i_{source.a} = AV_a \cdot i_{o.a}\left(exp\left(\frac{2F\cdot\eta_{act.a}}{RT}\right) - \frac{p_{H_2}}{p_{H_2.ref}}exp\left(\frac{-2F\cdot\eta_{act.a}}{RT}\right)\right) \tag{7}$$

$$i_{source.c} = AV_c \cdot i_{o.c}\left(\frac{p_{H_2O}}{p_{H_2O.ref}}exp\left(\frac{2F\cdot\eta_{act.c}}{RT}\right) - \frac{p_{O_2}}{p_{O_2.ref}}exp\left(\frac{-2F\cdot\eta_{act.c}}{RT}\right)\right) \tag{8}$$

The exchange current densities for the cathode ($i_{o.c}$) and the anode ($i_{o.a}$) are set at 4000 A m^{-2} and 1300 A m^{-2}, respectively [23]. The electrochemically active specific surface area of anode (AV_a) is fitted to be 2.33×10^5 m^{-1} and AV_c as 2.46×10^5 m^{-1} for cathode [21,24]. The electron conduction in the electron conducting Ni and SSC phases is governed by the Ohm's law (Eq.

9) to correlate the current distribution and electrical potential distribution by the local effective conductivity $\sigma_{l.eff}$. Similarly, the proton conduction in the BCZY phase is governed by Eq. 10:

$$i_s = -\sigma_{s.eff}\nabla(\emptyset_s),\ \nabla i_s = Q_s - i_{source} \quad (9)$$

$$i_l = -\sigma_{l.eff}\nabla(\emptyset_l), \nabla i_l = Q_l + i_{source} \quad (10)$$

The values of effective conductivities (electron conductivity $\sigma_{s.eff}$ and proton conductivity $\sigma_{l.eff}$) are obtained by the Bruggeman correction of their intrinsic conductivities considering the electrode tortuosity and porosity [25, 26]. In the composite electrode layers, the local electrical potentials in each phase ($\emptyset_l$ and $\emptyset_s$ for proton conducting phase and electron conducting phase, respectively) at the three boundary phase is assumed to correlate with various potential losses:

$$\emptyset_l - \emptyset_s = E_{H_2} - \eta_{act.a} - \eta_{act.c} - \eta_{conc.a} - \eta_{conc.c} \quad (11)$$

The operating voltage is applied at the cathode surface as the local $\emptyset_s$ with the anode surface being set as the ground ($\emptyset_s = 0$).

2.2 Mass transport model

As the dominating chemical reaction in the H-SOFC, the reaction rate of DMR acquires to be accurately calculated, as the DMR is the main reaction for the production of H_2 and CO, which subsequently influences the electrochemical current in the DMR-SOFC section. The general Langmuir-Hinshelwood-Hougen-Watson rate expression [27] is adopted here to determine the reaction rate at varied temperature and pressure:

$$R_{DMR} = K_0 \frac{k_1 k_2 K_1 P_{CH_4} P_{CO_2}}{k_1 K_1 P_{CH_4} P_{CO_2} + k_1 P_{CH_4} + k_2 K_1 P_{CO_2}}, (mol\ kg^{-1} s^{-1}) \quad (12)$$

The coefficient K_0 is fitted to be 0.167 by the characterization work of NiCo-CeO_2/ZrO_2 [28]. The volume-based mass loading of the catalyst is 5750 kg m^{-3} for the DMR reforming layer. Therefore, the mass-based rate expression R_{DMR} (mol kg^{-1} s^{-1}) can be implemented in the mass conversation and species conservation equations in the volume-based unit of mol m^{-3} s^{-1}:

$$\nabla \cdot (\rho U) = \sum \mathrm{M}_i R_i \tag{13}$$

$$\nabla \cdot \left(-\rho w_i \sum_{j=1}^{n} D_{eff,ij} \left(\nabla x_j + (x_j - w_j) \cdot \nabla P \cdot P^{-1}\right) + \rho w_i U\right) = R_i \tag{14}$$

, where the $D_{eff,ij}$ is the binary effective diffusion coefficient calculated by the dusty gas diffusion theory [29] indexed by species i and j. The x_j is the molar fraction of species j, while the w_j is the mass fraction. Besides R_{DMR}, R_i also represents the rates of other reactions involved, which includes R_{WGSR} and R_{MSR} [29], determined by:

$$R_{WGSR} = K_{sf}\left(p_{H_2O}p_{CO} - \frac{p_{H_2}p_{CO_2}}{K_{ps}}\right), (mol\, m^{-3}s^{-1}) \tag{15}$$

$$R_{MSR} = K_{rf}\left(p_{CH_4}p_{H_2O} - \frac{p_{CO}(p_{H_2})^3}{K_{pr}}\right), (mol\, m^{-3}s^{-1}) \tag{16}$$

To this end, the transport of gas species can be modelled by Eq. 14, assuming that the R_{DMR} is applied to the DMR layer; R_{WGSR} and R_{MSR} applied to both the DMR layer and fuel electrode, and the electrochemical consumption rate of H_2 to the fuel electrode.

2.3 Momentum transport model and heat transport model

Incompressible laminar flow is assumed for the gas flow in channels. The momentum transport equation in the porous electrodes can be written as:

$$\frac{\rho}{\varepsilon}\left((U \cdot \nabla)\frac{U}{\varepsilon}\right) = \nabla \cdot \left[-p + \frac{\mu}{\varepsilon}(\nabla U + (\nabla U)^T) - \frac{2}{3}\frac{\mu}{\varepsilon}(\nabla \cdot U)\right] - \mu\kappa^{-1}U \tag{17}$$

The heat transport equation can be written as:

$$\left(\rho c_p\right)_{eff} U \cdot \nabla T + \nabla\left(-\lambda_{eff}\nabla T\right) = Q_{heat} \tag{18}$$

The effectivity thermal conductivity of porous media would be determined based on the thermal conductivity, porosity and the density of the solid phase and flow phase. Q_{heat} is the heat source term from reactions (e.g. DMR, WGSR and MSR), as well as electrochemical heat sources, including the Ohmic heating, activation heating and other irreversible heat dissipation.

2.4 Validation

By coupling the governing equations introduced above, the multi-physical model is developed on the COMSOL V4.5 platform and solved by the Finite Element Method. The calculation procedures and the numerical details have been reported in our previous publication and are thus not included in the paper to avoid duplication. Interested readers can find the details in ref. [14,21,22]. Firstly, comprehensive validations of this model are carried out by two sets of comparisons: 1) the dry reforming catalyst kinetics characterization vs. simulation; 2) the button SOFC current-voltage curves measurement vs. simulation. Regarding the dry methane reforming catalytic activity, the kinetics of NiCo-CeO_2/ZrO_2 catalyst used in this model are validated by developing an isothermal model for a cylinder-shaped reactor of dry methane reforming and comparing the simulated CH_4 conversion ratio and CO_2 conversion ratio with the measured values from [28], The reactor is fed by CH_4:CO_2=1:1 in volume from 550 °C to 800 °C, as shown in Fig. 2a. The comparison in Fig. 2b shows a good agreement with the experimental results, being less than the maximum values calculated at thermodynamic state. On the other hand, the validation of the electrochemical and chemical reactions model (including the two half electrochemical reactions, WGSR and MSR) is realized by comparing voltage-current curves of a button H-SOFC which is comprehensively characterized [24] as shown in Fig. 2c. Additionally, the validation of WGSR and MSR rate models on Ni can also be found in our previous publication (Case I to IV in Table II of [22]). Based on the two validations mentioned above, the multi-physical model is considered to be capable of accurately simulating the co-generation processes in the studied DMR coupled H-SOFC.

3. Operating parameters and boundary conditions

To understand the effects of H_2O addition in the fuel, the base case operating conditions (with vs. without 20% H_2O assisting for CH_4 and CO_2 mixture at 0.7 V) are shown in Table 1. The boundary conditions are shown in Fig. 1. The applied potential of the cathode external surface

is specified as 0.7 V and the electrical ground is specified at the internal surface of DMR reforming layer. To eliminate the end effect of flows at inlets of the SOFC that would cause numerical errors, the inlets are extended for an additional 4 cm region, which are included into the computation domains and wrapped by thermal-insulated walls.

After the base case simulation, 3 sets of sensitivity studies were carried out to fully understand the effects of operating conditions, viz., H_2O fraction, operating voltage and fuel flow rate. Table 2 summarizes the ranges of those operating parameters.

4. Results and discussion

4.1 Base case analysis (with vs. without 20% H_2O operating)

In the case without H_2O, the comparison of the inlet gas composition and outlet composition is shown in Fig.3a and Fig. 3b. Nearly 7.1% CH_4 and 7.7% CO_2 still remain at the outlet, which corresponding to a CH_4 conversion ratio of 0.830. When 20% H_2O is used (see Fig. 3c), it is found from Fig. 3d that the fractions of CH_4 and CO_2 at the outlet are reduced to 4.4% and 0.6%, respectively. Beneficially, the molar fraction of H_2 is also largely improved (to 27.2%), which could be ascribed to the enhanced reforming of CH_4 by H_2O. The content of residual H_2O is found to be 4.4% that can be easily condensed and removed, thus not degrading the quality of produced syngas. Details of the SOFC performance are summarized in Table 3. It is worth noting that the added 20% H_2O also has a positive effect on the average current density (improved from 2832 to 3064 A cm^{-2}), being consistent with the current density distribution curves along the tubular cell at the mid cutline of the electrolyte layer (Fig. 3e). The insert 2D plots of current density distribution also reveal that the electrolyte phase current density (attributed to the transport of protons), gradually decreases along the flow direction, while quickly decays away from the electrolyte-electrode interface in the vertical direction. The authors view that the main reason for the current density difference between two cases could be due to the improved H_2 fraction, caused by the additional steam reforming of methane that

only occurs in the H_2O assisting case, supported by the H_2 fraction profile (Fig. 4b and Fig. 4d). The SOFC performance is also related to the temperature field. The simulated temperature profiles are shown in Fig. 3f. Slightly higher average temperature (949.85 K) in the tubular SOFC without H_2O is observed, compared to the 945.28 K of the 20% H_2O case as shown in Table 3. This could be due to the strong endothermic effect of MSR in the case of 20% H_2O case. Considering that higher working temperature usually has a positive effect on current density, but now the 20% H_2O assisting SOFC demonstrates a higher current density with a lower average temperature, it could be concluded that the origin of current enhancement observed should not be the temperature, but only the higher H_2 molar fraction due to steam reforming of CH_4. To further verify the role of H_2O in improving H_2 fraction and further improving the current density, species fraction distributions are profiled in Fig. 4a and 4b. The solid red line in Fig. 4a represents the CH_4 fraction of the 20% H_2O assisting case, showing that the CH_4 fraction is more quickly lowered down, starting from the DMR section compared to the dashed red line, which represents the No-H_2O case. This difference results from the enhanced MSR rate (R_{MSR}) denoted by the black lines (solid and dash) in Fig. 4d, although the DMR rate (R_{DMR}) are suppressed in the case of H_2O assisting. As these two reforming reactions are jointly responsible for the H_2 and CO production considering that the magnitudes of their rates are much higher than that of WGSR (R_{WGSR}, as shown in Fig. 4c), it can be observed that the H_2 fraction (solid cyan line in Fig. 4b) is improved to a larger extent in the DMR section, thus facilitating the H_2 electrochemical reaction in the DMR-SOFC section. Therefore, the H_2 fraction is expected to be consumed at a larger rate. In addition to the lower R_{DMR} in the DMR-SOFC section of the 20% H_2O case, the H_2 fraction profile consequently decreases at a steeper descending slope as verified by Fig. 4b. Similarly, the CO fraction of the 20% H_2O assisting case is also higher in the DMR section and lower than the No-H_2O case in the DMR-SOFC section, where the R_{MSR} decays to nearly zero due to the depletion of H_2O (as shown by the

solid black line in Fig. 4b). Based on the results discussed above, the enhancement effects of H_2O on 1) the CH_4 conversion and 2) syngas/power co-generation of SOFC is clearly presented by the simulation results of 20% H_2O assisting at 0.7 V operating. The enhancement is mainly explained by the improved methane reforming reaction from the additional steam reforming (R_{MSR}) in the DMR section. CH_4 conversion is greatly improved from 0.830 to 0.898; the current density of SOFC is improved from 2832 A m^{-2} to 3064 A m^{-2} that leads to a power generation improvement of 8.4%.

4.2 Sensitivity of H_2O fraction

As shown in the base case analysis, the performance of the SOFC is enhanced by the H_2O addition. It is necessary to investigate its sensitivity to the amount of H_2O, that could be practically advisable to the optimization of the SOFC. Fig. 5 shows the simulated results at varied H_2O molar fraction of the inlet fuel gas as prescribed by Case S1 in Table 2 from 0% to 50% with 10% stepping. The opposite trends of CO production rate and H_2 production rate are observed in Fig. 5a that the highest CO production rate is achieved at ca. 1.42×10^{-5} mol s^{-1} without H_2O assisting, while the highest H_2 production rate is achieved at ca. 8.09×10^{-6} mol s^{-1} with 50% H_2O assisting, i.e. the input gas is of a stoichiometric composition for steam reforming: CH_4:H_2O=1:1, without the participation of CO_2. As already explained in the base case analysis, these opposite trends should be explained by the enhanced R_{MSR} and the suppressed R_{DMR}. In this regard of more H_2 generated, the current density is increased by 22.5% from 2788.8 A m^{-2} (0% H_2O case) to 3426.5A m^{-2} (50% H_2O case). Fig. 5b provides the CH_4 conversion ratio and CO_2 conversion ratio when increasing the H_2O fraction. It should be noted that there exists an optimal H_2O fraction at ca. 20% when the maximum CH_4 conversion ratio can be achieved at ca. 0.898. In terms of CO_2 conversion ratio, it approaches 1.0 when the inlet CO_2 is gradually replaced by the H_2O.

By this study on the sensitivity of H_2 fraction, the authors recommend to adjust the value of H_2O fraction to be larger than 20% based on overall considerations of efficient CH_4 and CO_2 conversion and a desirable H_2:CO ratio (< 1) of the produced syngas for the synthesis of high value hydrocarbons.

4.3 Sensitivity of operating voltage

In this section, the effects of operating voltage are compared between the H_2O assisting case and No-H_2O case. The voltage-current curves in Fig. 6a clearly show that the simulated current density of the H_2O assisting case is higher when the operating voltage is lower than 0.6 V. This is indicative of the reduced concentration overpotential with H_2O assisting, that originates from the higher fraction of H_2. As verified by in Fig. 6b, the H_2 production rate is higher in the H_2O assisting case (solid cyan line), especially when operating voltage is lower than 0.6 V, so that the depletion of H_2 relieved to some extent.

Influenced by the enhanced electrochemical utilization of H_2, the conversion ratios of CO_2 and CH_4 in Fig. 6c are significantly improved as the higher current density would promote the reforming of CH_4 and CO_2 due to the equilibrium shifting of MSR and DMR to the left hand side. For example, at 0.5 V, the conversion ratios of both CH_4 and CO_2 are more than 0.97. Overall, the comparison of conversion ratios between the No-H_2O case and 20% H_2O case again confirms the positive effect of H_2O assisting not only at the base case (0.7 V) condition, but also in the whole voltage range from 0.5 to 0.9 V.

Concluding from this sensitivity study, it is more beneficial to introduce H_2O to assist the reforming of methane in the case of the high power output operating (lower voltage and higher current), because the enhanced H_2 production can help relieve the starvation of H_2 in the SOFC, thus lowering down overpotentials.

4.4 Sensitivity of fuel flow rate

The sensitivity of fuel flow rate is investigated in this section. The measured conversion ratios of CH_4 and CO_2 at three different flow rates: 50, 100 and 200 SCCM according to Case S3. It can be seen from Fig. 7 that the increase of anode flow can simply increase the current density, but the conversion ratios of CH_4 and CO_2 are both reduced. This can be explained by the insufficient catalyst loading for DRM and MSR at the current dimension of SOFC. Therefore, the excessive fuelling of CH_4 and CO_2 inevitably dilutes the H_2 and CO produced.

5. Conclusions

In this work, the effects of H_2O assisting on CH_4 reforming and SOFC performance are investigated. It shows that H_2O assisting is beneficial to the syngas and power co-generation in an H-SOFC by a 2D axisymmetric numerical model. It's found that 20% H_2O assisting can improve CH_4 conversion from 0.830 to 0.898 and the current density from 2832 A m^{-2} to 3064 A m^{-2} at 0.7 V that corresponds to a power generation improvement of 8.4%. The analysis of species distribution and chemical reforming rates from the modelling work attributes the improvement mainly to the synergies of combining dry methane reforming and methane steam reforming. Sensitivity studies of operating conditions, including H_2O fraction, operating voltage and fuel flow rate, are carried out. It is found that 1) the produced syngas composition is greatly influenced by the amount of H_2O used for assisting. Specifically, the higher fraction of H_2O leads to the higher H_2:CO ratio in the syngas, as well as the higher current density; 2) the assisting of H_2O can effectively reduce the concentration overpotential at a relative low voltage (<0.6 V) by relieving the H_2 starvation; 3) the conversion ratio of CH_4 and CO_2 is restricted by the reforming capacity of anode, which can be measured by catalyst loading mass vs. inlet fuel flow rate. Therefore, the dilution issue of H_2 by the inlet flue (CH_4/CO_2/H_2O) in such a non-H_2 fuelled proton SOFC system is more critical when increasing the flow rate.

Acknowledgements

This research is supported by a grant under the Theme-based Scheme (project number: T23-601/17-R) from Research Grant Council, University Grants Committee, Hong Kong SAR.

References

[1] Wu Y, Liao Y, Liu G, Ma X. Syngas production by chemical looping gasification of biomass with steam and CaO additive. Int J Hydrogen Energy 2018;43:19375–83.

[2] Toledo TM, Araus SK, Vasconcelo AD. Syngas production from coal in presence of steam using filtration combustion, Int J Hydrogen Energy 2015;40:6340–45.

[3] Huang Q, Wang J, Qiu K, Pan Z, Wang S. Catalytic pyrolysis of petroleum sludge for production of hydrogen-enriched syngas. Int J Hydrogen Energy 2015;40:16077–85.

[4] Zhang G, Liu J. Xu Y, Sun Y. A review of CH_4–CO_2 reforming to synthesis gas over Ni-based catalysts in recent years (2010–2017). Int J Hydrogen Energy 2018;43:15030–54.

[5] Hegarty MES, O'Connor AM, Ross JRH. Syngas production from natural gas using ZrO_2-supported metals. Catal Today 1998;42:225–32.

[6] Kathe M, Empfield A, Sandvik P, Fryer C, Zhang Y, Blair E, et al. Utilization of CO_2 as a partial substitute for methane feedstock in chemical looping methane–steam redox processes for syngas production. Energy Environ Sci 2017;10:1345–9.

[7] Ni M. Modeling of SOFC running on partially pre-reformed gas mixture. International Journal of Hydrogen Energy 2012; 37(2):1731-1745.

[8] Hanna J, Lee WY, Shi Y, Ghoniem AF. Fundamentals of electro-and thermochemistry in the anode of solid-oxide fuel cells with hydrocarbon and syngas fuels. Prog Energy Combust Sci 2014;40:74–111.

[9] Ni M. Modeling and parametric simulations of solid oxide fuel cells with methane carbon dioxide reforming. Energy Conversion and Management 2013;70:116–129.

[10] Sameshima S, Furukawa N, Hirata Y, Shimonosono T. Cell performance of SOFC using CH_4–CO_2 mixed gases. Ceram Int 2014;40:6279–84.

[11] Mishina T, Miya K, Kikuchi R, Sugawara T, Takagaki A, Oyama ST. Ni-SDC based cermets for direct dry reforming of methane on SOFC anode. ECS Trans 2017;78:1161–7.

[12] Wan T, Zhu A, Guo Y, Wang C, Huang S, Chen H, et al. Co-generation of electricity and syngas on proton-conducting solid oxide fuel cell with a perovskite layer as a precursor of a highly efficient reforming catalyst. J Power Sources 2017;348:9–15.

[13] Hua B, Yan N, Li M, Zhang Y, Sun Y, Li J, et al. Novel layered solid oxide fuel cells with multiple-twinned $Ni_{0.8}Co_{0.2}$ nanoparticles: the key to thermally independent CO_2 utilization and power-chemical cogeneration. Energy Environ Sci 2016;9:207–15.

[14] Chen B, Xu H, Sun Q, Zhang H, Tan P, Cai W, et al. Syngas/power cogeneration from proton conducting solid oxide fuel cells assisted by dry methane reforming: A thermal-electrochemical modelling study. Energy Convers Manag 2018;167:37–44.

[15] Gangadharan P, Kanchi KC, Lou HH. Chemical engineering research and design evaluation of the economic and environmental impact of combining dry reforming with steam reforming of methane. Chem Eng Res Des 2012;90:1956–68.

[16] Finnerty CM, Coe NJ, Cunningham RH, Ormerod RM. Carbon formation on and deactivation of nickel-based/zirconia anodes in solid oxide fuel cells running on methane. Catal Today 1998;46:137–45.

[17] Li Y, Wang Y, Zhang X, Mi Z. Thermodynamic analysis of autothermal steam and CO_2 reforming of methane. Int J Hydrogen Energy 2008;33:2507–14.

[18] Samuel P. GTL technology-Challenges and opportunities in catalysis. Bull Catal Soc India 2003;2:82–99.

[19] Zhao J, Xu X, Zhou W, Blakey I, Liu S, Zhu Z. Proton-conducting La-doped ceria-based internal reforming layer for direct methane solid oxide fuel cells. ACS Appl Mater Interfaces 2017;9:33758–65.
[20] Hua B, Li M, Pu J, Chi B, Jian L. $BaZr_{0.1}Ce_{0.7}Y_{0.1}Yb_{0.1}O_{3-\delta}$ enhanced coking-free on-cell reforming for direct-methane solid oxide fuel cells. J Mater Chem A 2014;2:12576–82.
[21] Chen B, Xu H, Zhang H, Tan P, Cai W, Ni M. A novel design of solid oxide electrolyser integrated with magnesium hydride bed for hydrogen generation and storage–A dynamic simulation study. Appl Energy 2017;200:260–72.
[22] Chen B, Xu H, Chen L, Li Y, Xia C, Ni M. Modelling of one-step methanation process combining SOECs and Fischer-Tropsch-like reactor. J Electrochem Soc 2016;163:F3001–8.
[23] Ni M, Leung MKH, Leung DYC. Electrochemical modeling of hydrogen production by proton-conducting solid oxide steam electrolyzer. Int J Hydrogen Energy 2008;33:4040–4047.
[24] He F, Song D, Peng R, Meng G, Yang S. Electrode performance and analysis of reversible solid oxide fuel cells with proton conducting electrolyte of $BaCe0_{.5}Zr_{0.3}Y_{0.2}O_{3-\delta}$. J Power Sources 2010;195:3359–64.
[25] Chen B, Xu H, Ni M. Modelling of SOEC-FT reactor: Pressure effects on methanation process. Appl Energy 2017;185:814–24.
[26] Ni M. 2D thermal modelling of a solid oxide electrolyzer cell (SOEC) for syngas production by H2O/CO2 co-electrolysis. International Journal of Hydrogen Energy 2012; 37(8): 6389-6399.
[27] Abashar MEE. Coupling of steam and dry reforming of methane in catalytic fluidized bed membrane reactors. Int J Hydrogen Energy 2004;29:799–808.
[28] Djinović P, Osojnik črnivec IG, Erjavec B, Pintar A. Influence of active metal loading and oxygen mobility on coke-free dry reforming of Ni-Co bimetallic catalysts. Appl Catal B Environ 2012;125:259–70.
[29] Haberman BA, Young JB. Three-dimensional simulation of chemically reacting gas flows in the porous support structure of an integrated-planar solid oxide fuel cell. Int J Heat Mass Transf 2004;47:3617–29.

Tables

Table 1 Base case operating with vs. without steam cases.

Parameters	**Values**
Fuel inlet composition	No-H_2O case: 50 SCCM; CH_4:CO_2=0.5:0.5 20% H_2O case: 50 SCCM; CH_4:CO2:H_2O=0.5:0.3:0.2
Air inlet composition	Air with 3% steam, 40 SCCM
Inlet temperature (K)	973
SOFC operating voltage (V)	0.7
Operating pressure (atm)	1.0

Table 2 Operating conditions of sensitivity studies (S1-S3).

Case name	**Varying parameters**	**Range**
S1	H_2O fraction	0% to 50% with 10% stepping
S2	Operating voltage	0.5 V to 0.9 V
S3	Fuel flow rate	50;100; 200 SCCM

Table 3 Summarization of the base case operating: with vs. without 20% H_2O.

Parameters	**Without H_2O**	**With 20% H_2O**
Average current density, A m^{-2}	2832	3064
Electricity output, W	1.54	1.67
CO_2 conversion	0.825	0.975
CH_4 conversion	0.830	0.898
Outlet H_2:CO ratio	0.19	0.43
Cell average temperature, K	949.85	945.28

Figures

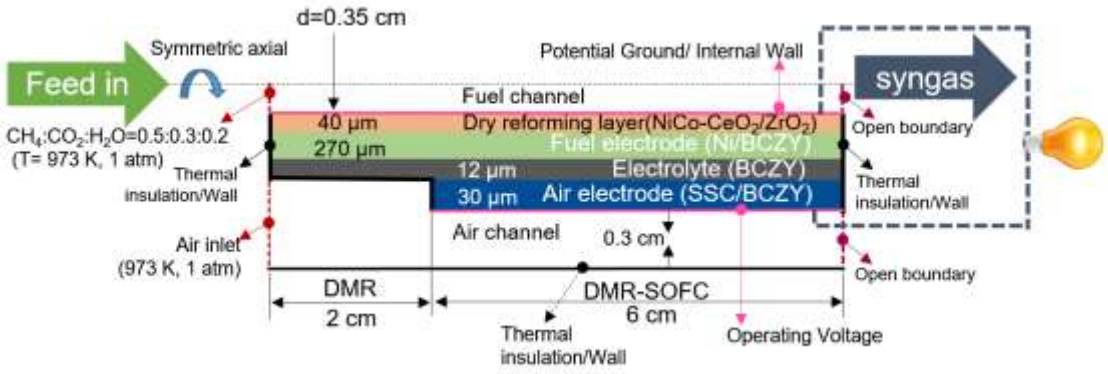

Fig. 1. The schematic of the designed H-SOFC with a dry methane reforming layer, divided as a DMR section and a DMR-SOFC section.

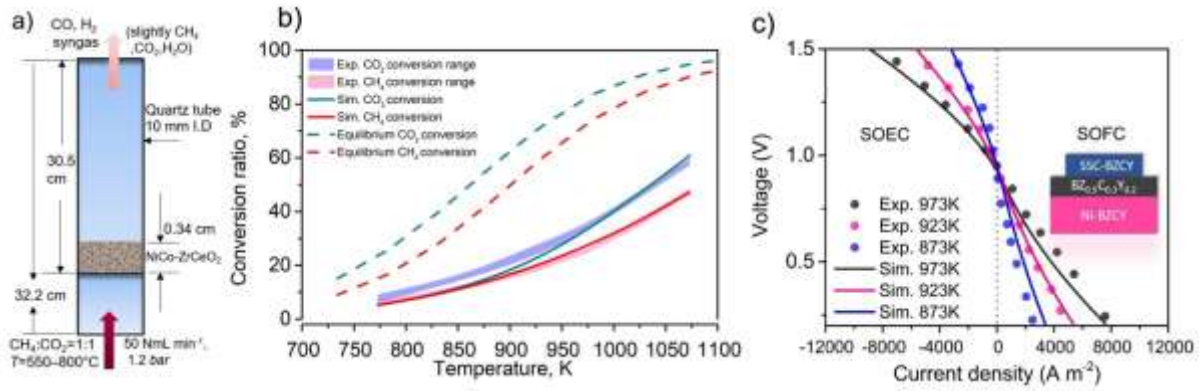

Fig. 2. (a) Schematics of the experimental testing; (b) experimental, simulated and equilibrium values of CH_4 and CO_2 conversion ratio; (c) The current-voltage curves of the button cell [14]. Copyright 2018, Elsevier.

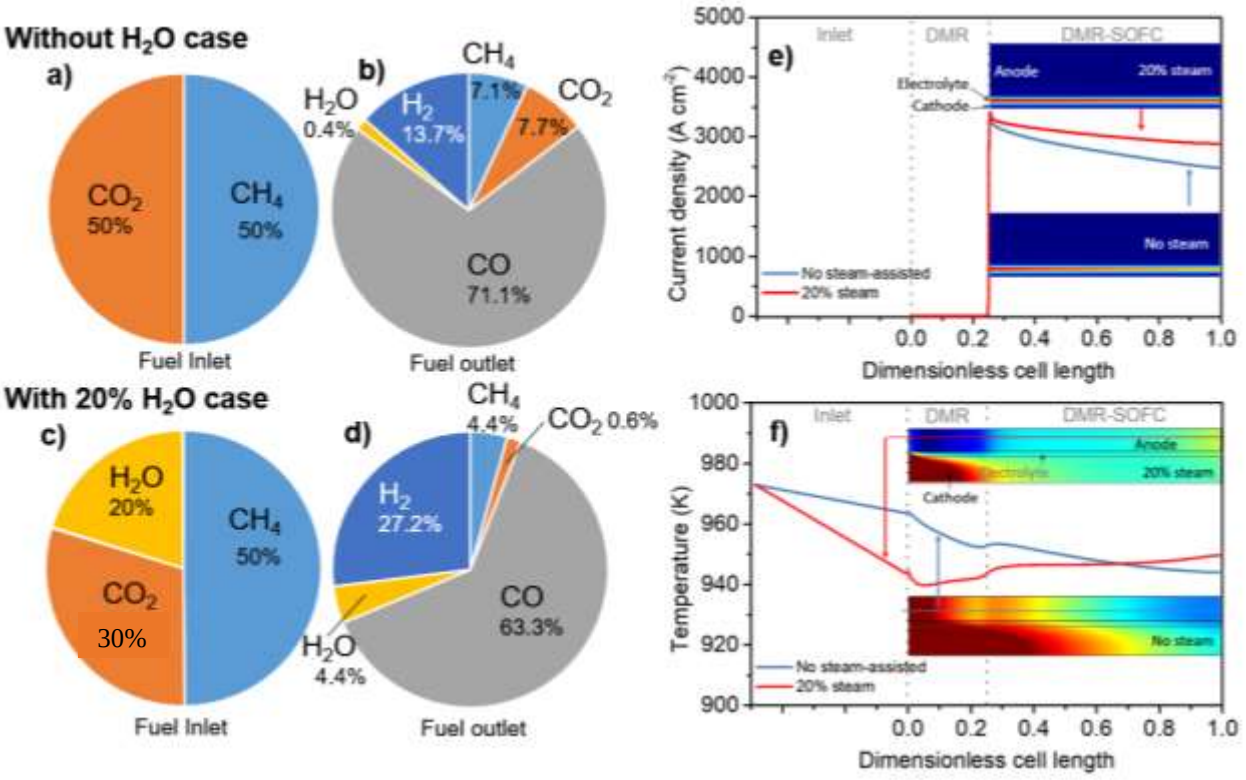

Fig. 3. Comparison of the fuel compositions at inlet and outlet, in the without H_2O case (a, b) and with 20% H_2O case (c, d); (e) the current density distribution along the SOFC flow direction at the mid line of electrolyte; (f) The temperature along the SOFC flow direction at the mid line of the fuel channel with the 2D distribution over the whole cell inserted.

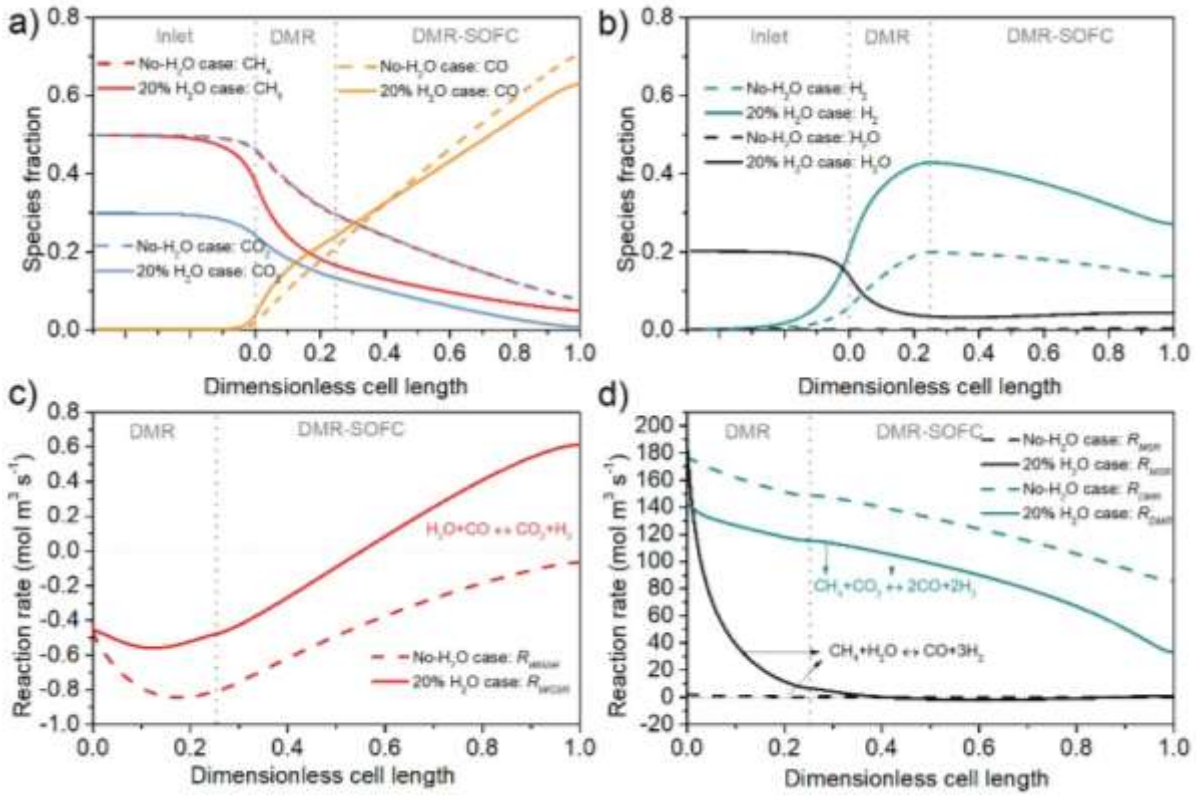

Fig. 4. (a) CH_4, CO_2 and CO fraction profile along the tubular SOFC from the inlet, DMR and DMR-SOFC section; (b) H_2 and H_2O fraction profile; (c) water gas shifting reaction rate (R_{WGSR}) profile at the mid cut line of the fuel electrode; (d) the methane steam reforming rate profile (R_{MSR}) and dry reforming reaction rate (R_{DMR}) profile at the mid cut line of the dry reforming layer.

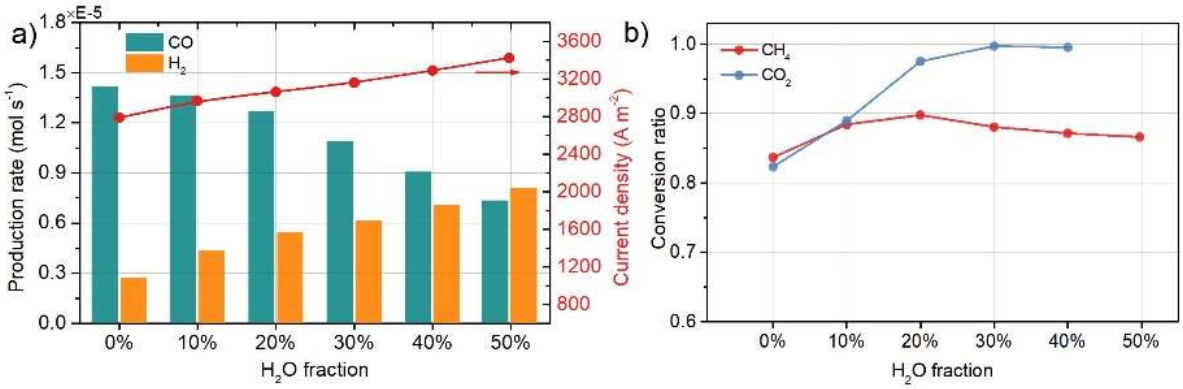

Fig. 5. (a) The production rate of CO and H_2, and current density at different H_2O fraction; (b) conversion ratios of CH_4 and CO_2.

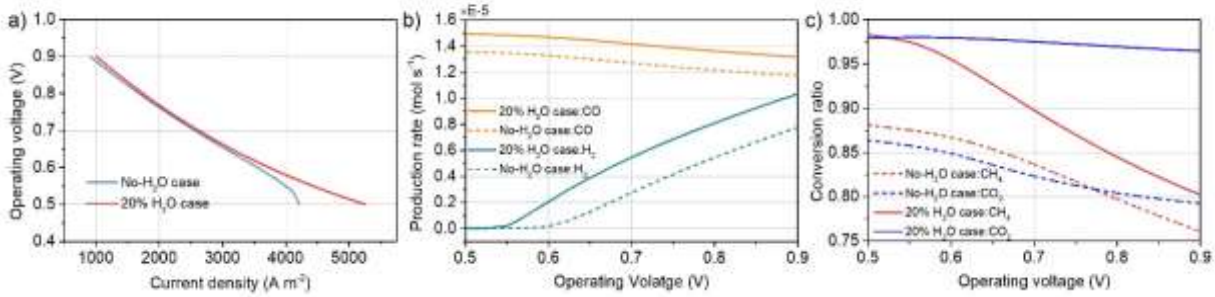

Fig. 6. (a) The voltage-current curves of No-H_2O case and 20% H_2O case of the SOFC; (b) the production rate of H_2 and CO; (c) the outlet conversion ratios of CH_4 and CO_2 at different operating voltage.

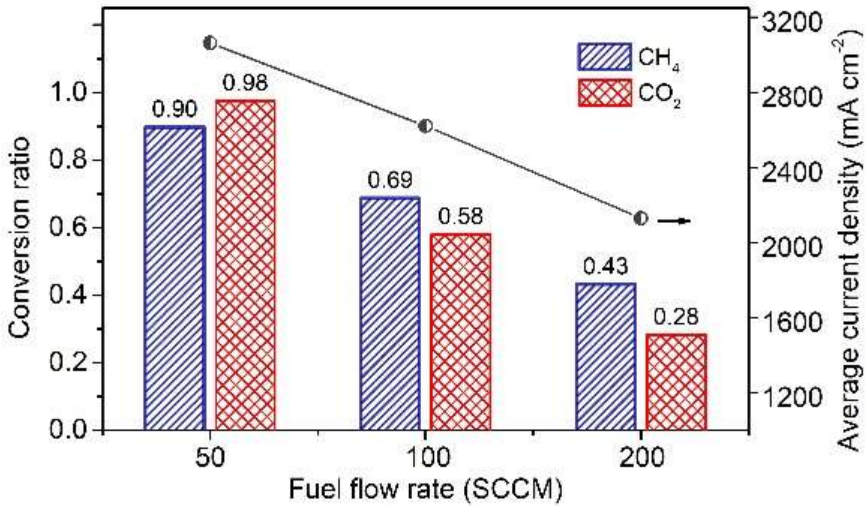

Fig. 7. The conversion ratios of CH_4 and CO_2, and current density at different fuel flow rates at 0.7 V with 20% H_2O assisting.